AD-A048 345 NAVAL UNDERWATER SYSTEMS CENTER NEW LONDON CONN NEW --ETC F/G 20/14
NUMERICAL RESULTS FOR MODIFIED IMAGE THEORY QUASI-STATIC RANGE --ETC(U)
DEC 77 P R BANNISTER, R L DUBE

UNCLASSIFIED NUSC-TR-5775 NL

| OF |

ADA048345

END

DATE FILMED

2-78

DDC

NUSC Technical Report 5775

Numerical Results for Modified Image Theory Quasi-Static Range Subsurface-to-Subsurface and Subsurface-to-Air Propagation Equations

Peter R. Bannister
Rene' L. Dube
Submarine Electromagnetic Systems Department

7 December 1977

NUSC
NAVAL UNDERWATER SYSTEMS CENTER
Newport, Rhode Island • New London, Connecticut

PREFACE

This report was prepared under NUSC Project No. A-532-24, P. R. Bannister, Principal Investigator; Naval Industrial Funding was from David W. Taylor Naval Ship Research and Development Center, W. J. Andahazy, Project Director. The sponsor was the Naval Sea Systems Command, Project Program Manager, W. L. Welsh, SEA 03424.

The Technical Reviewer for this report was J. J. Tennyson (Code 3403).

REVIEWED AND APPROVED: 7 December 1977

John Merrill

John Merrill
Head: Submarine Electromagnetic Systems Department

The authors of this report are located at the New London Laboratory, Naval Underwater Systems Center, New London, Connecticut 06320.

REPORT DOCUMENTATION PAGE		READ INSTRUCTIONS BEFORE COMPLETING FORM
1. REPORT NUMBER TR 5775	2. GOVT ACCESSION NO.	3. RECIPIENT'S CATALOG NUMBER
4. TITLE (and Subtitle) NUMERICAL RESULTS FOR MODIFIED IMAGE THEORY QUASI-STATIC RANGE SUBSURFACE-TO-SUBSURFACE AND SUBSURFACE-TO-AIR PROPAGATION EQUATIONS,		5. TYPE OF REPORT & PERIOD COVERED Technical rept.,
		6. PERFORMING ORG. REPORT NUMBER
7. AUTHOR(s) Peter R. Bannister René L. Dube		8. CONTRACT OR GRANT NUMBER(s)
9. PERFORMING ORGANIZATION NAME AND ADDRESS Naval Underwater Systems Center New London Laboratory New London, CT 06320		10. PROGRAM ELEMENT, PROJECT, TASK AREA & WORK UNIT NUMBERS A-532-24
11. CONTROLLING OFFICE NAME AND ADDRESS Naval Sea Systems Command SEA-03424 Washington, DC 20362		12. REPORT DATE 7 December 1977
		13. NUMBER OF PAGES 30
14. MONITORING AGENCY NAME & ADDRESS (if different from Controlling Office) (12) 31p.		15. SECURITY CLASS. (of this report) UNCLASSIFIED
		15a. DECLASSIFICATION/DOWNGRADING SCHEDULE

16. DISTRIBUTION STATEMENT (of this Report)

Approved for public release; distribution unlimited.

(14) NUSC-TR-5775

17. DISTRIBUTION STATEMENT (of the abstract entered in Block 20, if different from Report)

18. SUPPLEMENTARY NOTES

19. KEY WORDS (Continue on reverse side if necessary and identify by block number)

Dipole Antennas
Modified Image Theory
Quasi-Static Range
Numerical Integration Results
Subsurface-to-Air Propagation
Subsurface-to-Subsurface Propagation
Earth-Image Theory

20. ABSTRACT (Continue on reverse side if necessary and identify by block number)

Numerical results are presented for the previously derived horizontal electric dipole modified image-theory quasi-static range field component approximations. Both subsurface-to-subsurface and subsurface-to-air propagation cases are considered. It is shown that the modified image theory approximations are in good agreement with the more exact numerical integration results.

DD FORM 1 JAN 73 1473

405 918 LB

TABLE OF CONTENTS

Page

LIST OF ILLUSTRATIONS

LIST OF ILLUSTRATIONS (Cont'd)

NUMERICAL RESULTS FOR MODIFIED IMAGE THEORY QUASI-STATIC RANGE SUBSURFACE-TO-SUBSURFACE AND SUBSURFACE-TO-AIR PROPAGATION EQUATIONS

INTRODUCTION

During the past few years, considerable interest has been shown in determining the quasi-static field components of antennas located above or buried beneath the earth's surface. The quasi-static range is defined as the range where the measurement distance is much less than a free-space wavelength. Quasi-static range results are useful for submarine radio communication and detection as well as for the buried-miner problem. They are also helpful to geophysicists engaged in determining the electrical properties of the earth.

Some work has been done[1-5] on determining the quasi-static fields from various subsurface sources when the measurement distance $R = (\rho^2 + z^2)^{1/2}$ is comparable to the earth skin depth δ. However, the resulting field strength expressions are very complicated because they involve products of modified Bessel functions of different argument. Computing the field component expressions is lengthy and difficult, but some numerical results have been obtained. One method of obtaining these results has been discussed by Atzinger, Pensa, and Pigott.[6] Numerical integration techniques have also been employed.[7,8]

Recently,[9] by utilizing techniques of finitely conducting earth image theory, the authors have derived approximate expressions for the general quasi-static range electromagnetic fields produced by various subsurface antennas. It is the purpose of this report to provide some numerical calculations of these approximate field component expressions. The image-theory expressions are also compared with the more exact numerical integration results.

Physically, the essence of the finitely conducting earth-image theory technique is to replace the finitely conducting earth by a perfectly conducting earth located at the (complex) depth $d/2$, where $d = 2/\gamma = \delta(1-i)$. Analytically, this corresponds to replacing the algebraic reflection coefficient $(u-\lambda)/(u+\lambda)$ in the exact integral equations by $\exp(-\lambda d)$, where λ is the variable of integration.

For antennas located at or above the earth's surface, the general image theory approximation is valid throughout the quasi-static range.[10,11] However, if one or both antennas are buried, the previously derived[10] surface-to-surface and surface-to-air image-theory results, multiplied by the exponential attenuation-with-depth factor $\exp[\gamma(z + h)]$ or $\exp(\gamma h)$, generally will be valid only for $R > 3|z + h|$, where h and z, respectively, are the depth of the source and receiving antennas.

Therefore, we modified further the exact subsurface-to-subsurface and subsurface-to-air integral equations and obtained fairly simple field-strength equations[9] for the general quasi-static range, which reduce to previously derived results when $R >> \delta$ and when $R << \delta$ and $|z + h| << \delta$.

For the purposes of this report, we will consider a horizontal electric dipole (HED) source that is oriented in the x-direction and located at depth $h (h \leq 0)$ with respect to a cylindrical coordinate system (ρ, ϕ, z). The dipole is assumed to be of infinitesimal length ℓ and carry a constant current I. The earth occupies the lower half-space $(z < 0)$ and the air occupies the upper half-space $(z > 0)$. Displacement currents are neglected in both the ground and the air. The magnetic permeability of the earth is assumed to equal the permeability of free space μ_0. Meter-kilogram-second (MKS) units are employed and a suppressed time factor of $\exp(i\omega t)$ is assumed.

HORIZONTAL ELECTRIC DIPOLE (HED) FIELD COMPONENT EXPRESSIONS

The appropriate modified image-theory equations for HED subsurface-to-air-propagation $(h < 0, z > 0)$ are given on page 6 of the previous report[9] and are as follows:

$$E_\rho \sim \frac{I\ell \cos \phi e^{\gamma a h}}{2\pi\sigma K_1^3} \left\{1 + b - \frac{3b(z - bh)^2}{K_1^2} - \gamma a(z - bh)\right\}, \quad (1)$$

$$E_\phi \sim \frac{I\ell \sin \phi e^{\gamma a h}}{2\pi\sigma K_1^3} \left\{1 + \frac{2K_1^2}{d^2}\left(1 - \frac{K_1}{K_2}\right)\right\}, \quad (2)$$

$$E_z \sim \frac{I\ell \cos \phi e^{\gamma a h}}{4\pi\sigma} \left\{\frac{6\rho(z - bh)}{K_1^5} - \frac{4}{\rho d^2}\left[\frac{(z - bh)}{K_1} - \frac{(d + z - bh)}{K_2}\right]\right\}, \quad (3)$$

$$H_\rho \sim \frac{I\ell \sin\phi e^{\gamma ah}}{4\pi}\left\{\frac{(d + z - bh)}{K_2^3} - \frac{(z - bh)}{K_1^3} + \frac{1}{\rho^2}\left[\frac{(d + z - bh)}{K_2} - \frac{(z - bh)}{K_1}\right]\right\} , \quad (4)$$

$$H_\phi \sim - \frac{I\ell \cos\phi e^{\gamma ah}}{4\pi\rho^2}\left\{\frac{(d + z - bh)}{K_2} - \frac{(z - bh)}{K_1}\right\} , \quad (5)$$

and

$$H_z \sim \frac{I\ell\rho \sin\phi e^{\gamma ah}}{4\pi}\left\{\frac{1}{K_1^3} - \frac{1}{K_2^3}\right\} , \quad (6)$$

where

$K_1^2 = \rho^2 + (z - bh)^2$ and $K_2^2 = \rho^2 + (d + z - bh)^2$,
$a = 0$ and $b = 1$ for $R << \delta$ and $|h| << \delta$,
$a = 0.4$ and $b = 0.96$ for R/δ less than approximately 1,
$a = 0.96$ and $b = 0.4$ for R/δ between approximately 1 and 10, and
$a = 1.0$ and $b = 0$ for $R > |3h|$.

The appropriate modified image theory equations for HED subsurface-to-subsurface propagation ($h < 0$, $z < 0$), given on pages 13 and 14 of the previous report,[9] are

$$E_\rho \sim \frac{I\ell \cos\phi}{4\pi\sigma}\left\{\frac{e^{-\gamma R_0}}{R_0^3}\left[\left(\frac{3\rho^2}{R_0^2} - 1\right)\left(1 + \gamma R_0\right) - \gamma^2(z - h)^2\right] - \frac{e^{-\gamma R_1}}{R_1^3}\left[\left(\frac{3\rho^2}{R_1^2} - 1\right)\left(1 + \gamma R_1\right) - \gamma^2(z + h)^2\right] + \frac{2e^{\gamma a(z+h)}}{K_3^3}\left[1 + b - \frac{3b^3(z + h)^2}{K_3^2} + \gamma ab(z + h)\right]\right\} \quad (7)$$

$$E_\phi \sim \frac{I\ell \sin\phi}{4\pi\sigma}\left\{\frac{e^{-\gamma R_0}}{R_0^3}(1 + \gamma R_0 + \gamma^2 R_0^2) - \frac{e^{-\gamma R_1}}{R_1^3}(1 + \gamma R_1 + \gamma^2 R_1^2)\right.$$

$$\left. + \frac{2e^{\gamma a(z+h)}}{K_3^3}\left[1 + \frac{2K_3^2}{d^2}\left(1 - \frac{K_3}{K_4}\right)\right]\right\} , \qquad (8)$$

$$E_z \sim \frac{I\ell \cos\phi}{4\pi\sigma}\left\{\frac{\rho(z - h)}{R_0^5}(3 + 3\gamma R_0 + \gamma^2 R_0^2)e^{-\gamma R_0}\right.$$

$$\left. + \frac{\rho(z + h)}{R_1^5}(3 + 3\gamma R_1 + \gamma^2 R_1^2)e^{-\gamma R_1}\right\} , \qquad (9)$$

$$H_\rho \sim \frac{I\ell \sin\phi}{4\pi}\left\{-\frac{(z - h)}{R_0^3}(1 + \gamma R_0)e^{-\gamma R_0}\right.$$

$$\left. + e^{\gamma a(z+h)}\left[\frac{d - b(z + h)}{K_4\rho^2} + \frac{b(z + h)}{K_3\rho^2} + \frac{d - b(z + h)}{K_4^3}\right]\right\} , \qquad (10)$$

$$H_\phi \sim -\frac{I\ell \cos\phi}{4\pi}\left\{\frac{(z - h)}{R_0^3}(1 + \gamma R_0)e^{-\gamma R_0} + \frac{(z + h)}{R_1^3}(1 + \gamma R_1)e^{-\gamma R_1}\right.$$

$$\left. + \frac{e^{\gamma a(z+h)}}{\rho^2}\left[\frac{d - b(z + h)}{K_4} + \frac{b(z + h)}{K_3}\right]\right\} , \qquad (11)$$

and

$$H_z \sim \frac{I\ell\rho \sin\phi}{4\pi}\left\{\frac{e^{-\gamma R_0}}{R_0^3}(1 + \gamma R_0) - \frac{e^{-\gamma R_1}}{R_1^3}(1 + \gamma R_1)\right.$$

$$\left. + e^{\gamma a(z+h)}\left[\frac{1}{K_3^3} - \frac{1}{K_4^3}\right]\right\} . \qquad (12)$$

where

$$K_3^2 = \rho^2 + [b(z + h)]^2 \quad \text{and} \quad K_4^2 = \rho^2 + [d - b(z + h)]^2 \ ,$$

$$R_0^2 = \rho^2 + (z - h)^2 \quad \text{and} \quad R_1^2 = \rho^2 + (z + h)^2,$$

$a = 0$ and $b = 1$ for $R_1/\delta << 1$,
$a = 0.4$ and $b = 0.96$ for R_1/δ less than approximately 1,
$a = 0.96$ and $b = 0.4$ for R_1/δ between approximately 1 and 10, and
$a = 1$ and $b = 0$ for $\rho > 3|z + h|$.

NUMERICAL RESULTS

Note that we have defined loosely the variables a and b. That is, we let $a = 0.96$ and $b = 0.4$ for R_1/δ between approximately 1 and 10, and $a = 0.4$ and $b = 0.96$ for R_1/δ less than approximately 1. The specific crossover point for each field-strength component will depend not only on R_1/δ but also on $|z + h|/\delta$.

Because the resulting field-strength formulas can be calculated easily on a desk-top calculator, the field strengths can be determined by using both values of a and b, thus numerically determining the crossover point. Alternatively, we could set the two expressions (involving different values of a and b) equal and solve for the crossover point.

Comparisons of modified image theory and numerical integration results for the electric and magnetic fields in air (or earth) produced by a buried HED are presented in figures 1 through 28, which follow page 8. The normalized amplitude of each component (E' or H') is plotted versus ρ/δ for various values of $H(= h/\delta)$ and $Z(= z/\delta)$, where

$$H' = \frac{4\pi\delta^2 H}{I\ell \begin{Bmatrix}\sin\phi \\ \cos\phi\end{Bmatrix}} \quad \text{and} \quad E' = \frac{4\pi\sigma\delta^3 E}{I\ell \begin{Bmatrix}\sin\phi \\ \cos\phi\end{Bmatrix}} \ . \tag{13}$$

The normalization factor (0 dB) is the numerical integration value of each component at $\rho/\delta = 0.1$.

Presented in figures 1 and 2 are comparisons of the modified image theory and numerical integration results for the magnetic fields at a height of one skin depth ($Z = 1.0$) produced by an HED buried at a depth of one skin depth ($H = -1.0$). From figure 1, we see that the crossover point for this example is $\rho/\delta = 1.5$ ($R/\delta = 1.8$). That is, if $0.1 < \rho/\delta < 1.5$, then $a = 0.4$ and $b = 0.96$, whereas if $1.5 < \rho/\delta < 10$, then $a = 0.96$ and $b = 0.4$. A comparison (figure 2) of the composite modified image-theory results with the numerical integration results shows that the modified image-theory calculations are within approximately 1 dB of the numerical integration results over the complete range of ρ/δ (0.1 to 10). In fact, the modified image theory even predicts the H_ρ component amplitude dip at the right place ($\rho/\delta \sim 1.5$).

Comparisons of the modified image-theory and numerical integration results for the electric fields at a height of one skin depth produced by an HED buried at two skin depths (H = -2.0) are presented in figures 3 through 5. From figure 3, we see that the a = 0.96, b = 0.4 curve is in better agreement with the numerical integration result throughout the range of ρ/δ plotted. For values of $\rho/\delta > 3$, a much better fit to the numerical integration result can be obtained by letting a = 1 and b = 0. Alternatively, one could employ the quasi-near range formulas given in table 3.13 of Kraichman.[12]

From figure 4, we see that the a = 0.96, b = 0.4 curve is in good agreement with the numerical integration result for ρ/δ = 0.1 to 10. However, for the E_z^ζ component (figure 5), the crossover point is at $\rho/\delta \sim 1.5$. That is, if $0.1 < \rho/\delta < 1.5$, then a = 0.4 and b = 0.96, whereas if $1.5 < \rho/\delta < 10$, then a = 0.96 and b = 0.4.

Presented in figures 6 through 8 are comparisons of the modified image-theory and numerical integration results for the electric fields at a height of two skin depths produced by an HED buried at one skin depth. From these figures we observe that the a = 0.96, b = 0.4 curve is in excellent agreement with the numerical integration result throughout the range of ρ/δ considered (0.1 to 10).

It should be noted that because of reciprocity, the normalized electric field plots presented in figures 3 through 8 are also valid for air-to-subsurface propagation if Z and H are interchanged. That is, figures 3 and 4 also represent the horizontal electric field at a depth of two skin depth produced by a horizontal electric dipole located at a height of one skin depth, while figure 5 represents the horizontal electric field at a depth of two skin depths produced by a vertical electric dipole (VED) source at a height of one skin depth. For further details, see reference 9.

Comparisons of the modified image theory and numerical integration results for the magnetic fields at a height of two skin depths produced by an HED buried at one skin depth are presented in figures 9 through 11. From figure 9, we see that the crossover point for the H_ρ^ζ component is at $\rho/\delta \sim 2.2$. That is, if $0.1 < \rho/\delta < 2.2$, then a = 0.4 and b = 0.96, whereas if $2.2 < \rho/\delta < 10$, then a = 0.96 and b = 0.4. For the H_ϕ^ζ component (figure 10), the a = 0.96, b = 0.4 curve is in excellent agreement with the numerical integration result throughout the range of ρ/δ considered. From figure 11, we see that the crossover point for the H_z component is at $\rho/\delta \sim 1.5$.

Presented in figures 12 through 14 are comparisons of the modified image theory and numerical integration results for the magnetic fields at a height of one skin depth produced by a buried HED at a depth of two skin depths. From these figures, we see that the crossover point is $\rho/\delta \sim 2$ for the H_{ρ}' component (figure 12), $\rho/\delta \sim 0.8$ for the H_{ϕ}' component (figure 13), and $\rho/\delta \sim 1.7$ for the H_{z}' component (figure 14).

It should be noted that because of reciprocity, the normalized magnetic field plots presented in figures 9 through 14 are also valid for air-to-subsurface propagation if Z and H are interchanged. That is, figures 9 and 10 also represent the horizontal electric field at a depth of one skin depth produced by a horizontal magnetic dipole (HMD) source located at a height of two skin depths while figure 11 represents the horizontal electric field at a depth of one skin depth produced by a vertical magnetic dipole (VMD) source located at a height of two skin depths. For further details, see reference 9.

Comparisons of the modified image theory and numerical integration results for the electric and magnetic fields at a depth of one skin depth produced by an HED located at the earth's surface (H=0) are given in figures 15 through 19. From these figures, we see that the crossover point is $\rho/\delta \sim 1.5$ for the E_{ρ}' component (figure 15), $\rho/\delta \sim 1.0$ for the E_{ϕ}' component (figure 16), $\rho/\delta \sim 1.5$ for the H_{ρ}' component (figure 17), $\rho/\delta \sim 1.0$ for the H_{ϕ}' component (figure 18), and $\rho/\delta \sim 1.0$ for the H_{z}' component (figure 19). It should be noted that for $\rho/\delta > 3$, an even better fit to the numerical integration results can be obtained by setting $a = 1.0$ and $b = 0$. Alternatively, one could employ the quasi-near range formulas given in table 3.16 of Kraichman.[12]

Referring to equations (7) through (11), we see that, for the E_{ρ}', E_{ϕ}', and H_{z}' components, identical results will be obtained for the H=0, Z=-1 and H=-1, Z=0 cases. However, for the H_{ρ} and H_{ϕ} components, this will not be the case. This fact is further illustrated in figures 20 and 21, which present comparisons of the modified image-theory and numerical integration results for the horizontal magnetic fields at the surface (Z=0) produced by a HED buried at a depth of one skin depth (H=-1). From figure 20, we see that the $a = 0.96$, $b = 0.4$ H_{ρ}' curve is in fair agreement with the numerical integration result for $0.1 < \rho/\delta < 3$ and in very good agreement for $\rho/\delta > 3$. Referring to figure 21, we see that the crossover point for the H_{ϕ} component is at $\rho/\delta \sim 1.5$. That is, if $0.1 < \rho/\delta < 1.5$, then $a = 0.4$ and $b = 0.96$, whereas if $1.5 < \rho/\delta < 10$, then $a = 0.96$ and $b = 0.4$.

Presented in figures 22 and 23 are comparisons of the modified image theory and numerical integration results for the horizontal magnetic fields at a depth of one skin depth produced by a HED buried at one skin depth. From these figures we see that the crossover point for both components occurs at $\rho/\delta \sim 1.0$. It should be noted, however, that for the H_ϕ' component (figure 23), the a = 0.96, b = 0.4 curve is in good agreement with the numerical integration result throughout the range of ρ/δ considered.

Comparisons of the modified image theory and numerical integration results for the electric and magnetic fields at a depth of two skin depths, produced by an HED located at the earth's surface, are presented in figures 24 through 28. From these figures we see that the crossover point is at $\rho/\delta \sim 1$ to 1.5 for all five components. The agreement between the modified image theory and numerical integration results is very good for the H_ρ' and H_ϕ' components (figures 26 and 27) and fair for the E_ρ', E_ϕ', and H_z' components (figures 24, 25, and 28). The modified image theory fails to predict the E_ρ' amplitude dip at $\rho/\delta \sim 2.5$ (figure 24), although it did predict the E_ρ' amplitude dip for the H=0, Z=-1 case (figure 15). For both the E_ϕ' and H_z' components (figures 25 and 28), the a=0.4, b=0.96 curve is in good agreement with the numerical integration result from $0.1 < \rho/\delta < 3$. For $\rho/\delta > 3$, better results can be obtained by setting a=1.0 and b=0.

Because of reciprocity, the normalized electric and magnetic field plots presented in figures 15 through 28 are also valid for subsurface (or surface) to subsurface (or surface) propagation if Z and H are interchanged. That is, figures 15 and 16 also represent the horizontal electric fields at the surface produced by an HED buried at one skin depth; figures 17 and 18 also represent the horizontal electric fields at the surface produced by an HMD buried at one skin depth; and figure 19 also depicts the horizontal electric field at the surface produced by a buried VMD located at H=-1. Reference 9 contains further details.

CONCLUSIONS

Numerical results have been presented for the previously derived[9] HED modified image-theory quasi-static range subsurface-to-subsurface and subsurface-to-air propagation approximate field component expressions. It has been shown that, for the most part, the modified image-theory approximations are in good agreement with the more exact numerical integration results.

These modified image theory results will be useful for submarine radio communication and detection as well as for the buried miner problem. They also may be helpful to geophysicists engaged in determining the electrical properties of the earth.

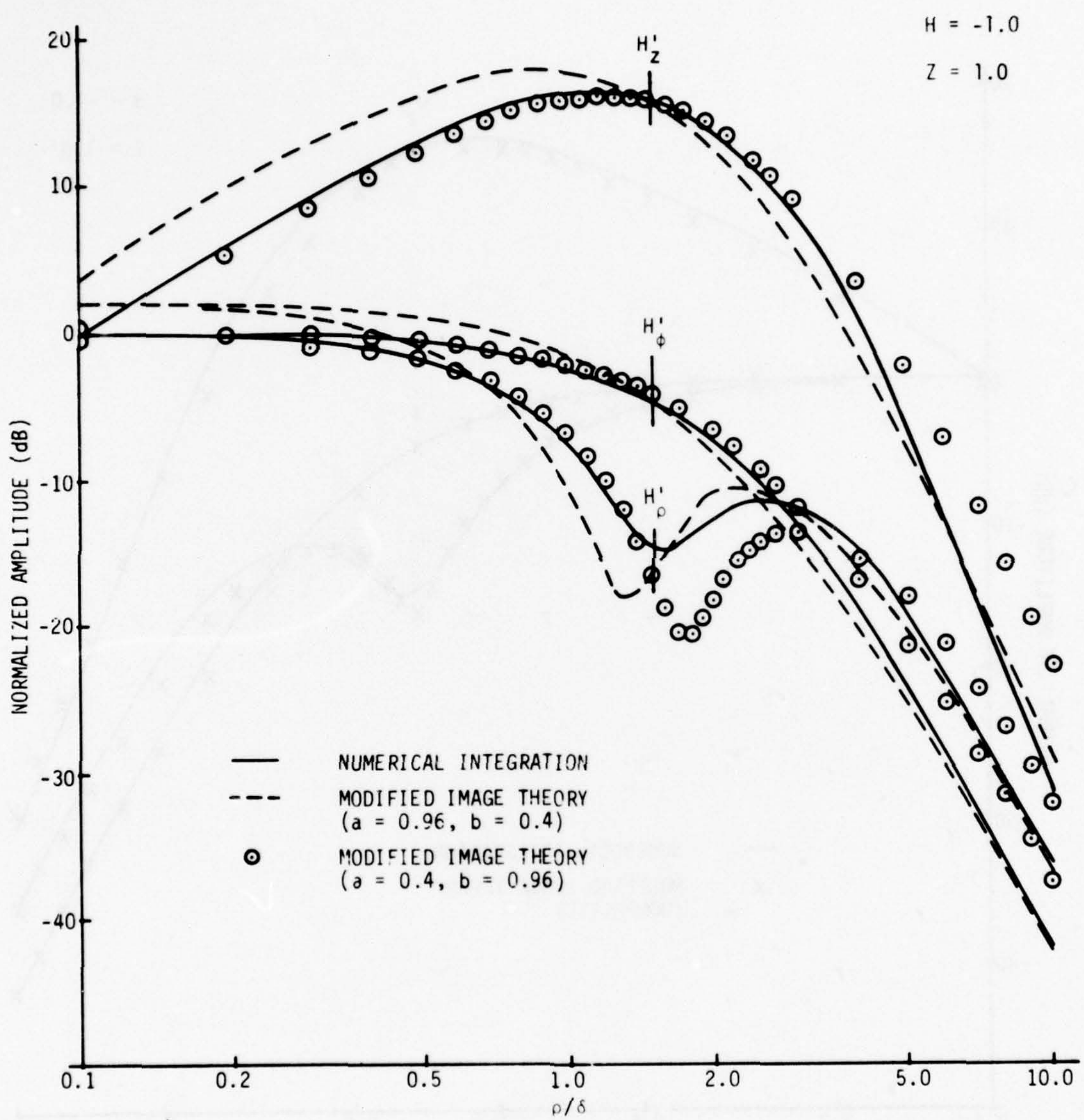

Figure 1. Comparison of Modified Image Theory and Numerical Integration Results for the Magnetic Fields in Air Produced by a Buried HED (H = -1.0, Z = 1.0)

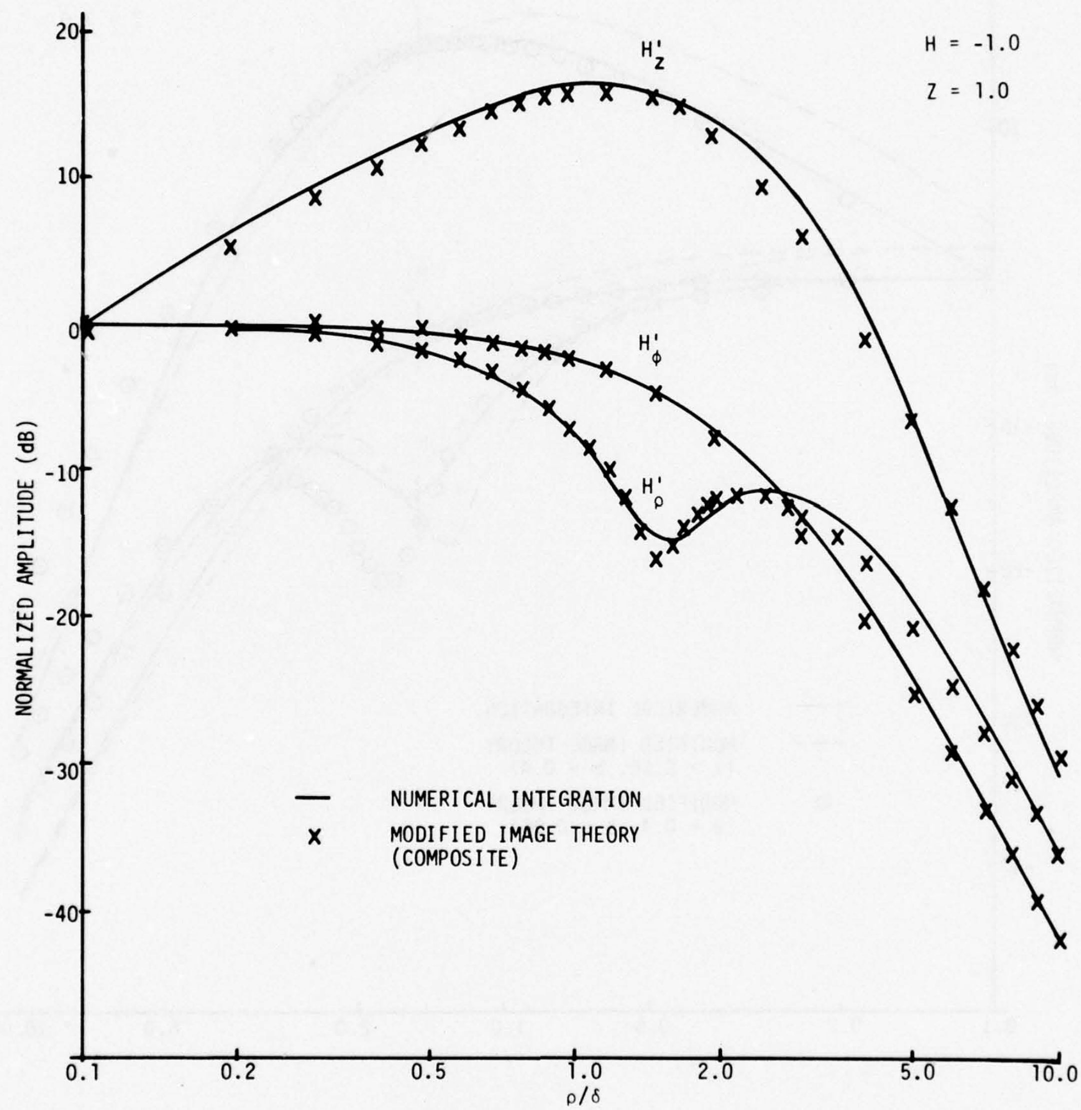

Figure 2. Comparison of Composite Modified Image Theory and Numerical Integration Results for the Magnetic Fields in Air Produced by a Buried HED (H = -1.0, Z = 1.0)

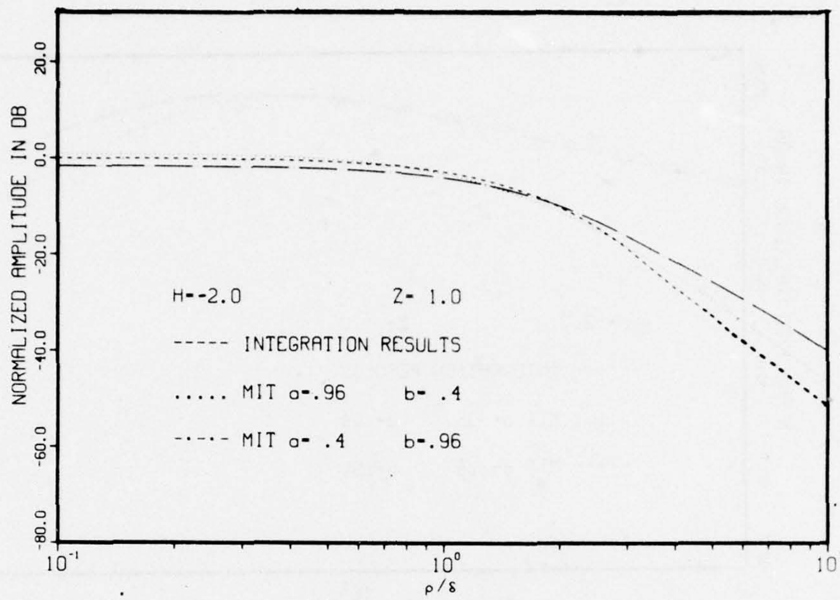

Figure 3. Comparison of Modified Image Theory and Numerical Integration Results for the E_ρ' Component in Air Produced by a Buried HED (H = -2.0, Z = 1.0)

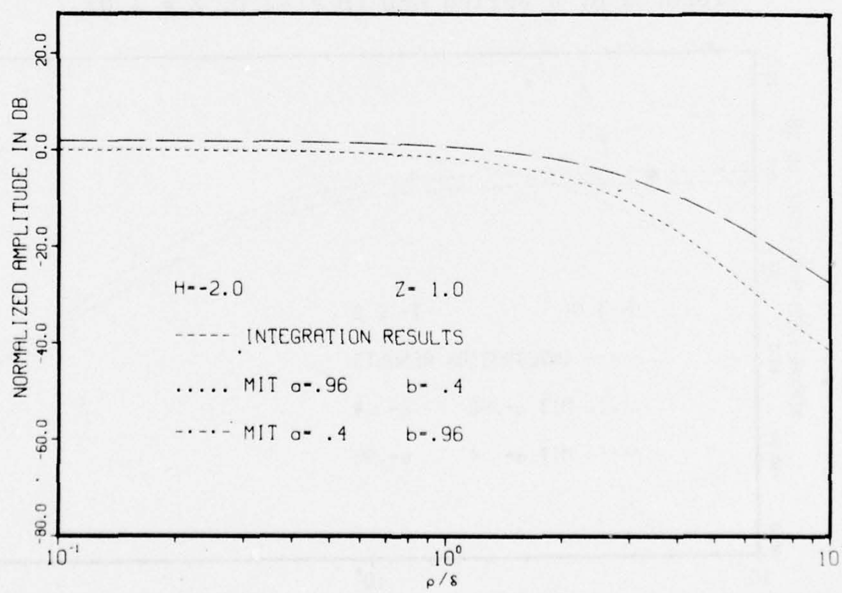

Figure 4. Comparison of Modified Image Theory and Numerical Integration Results for the E_ϕ' Component in Air Produced by a Buried HED (H = -2.0, Z = 1.0)

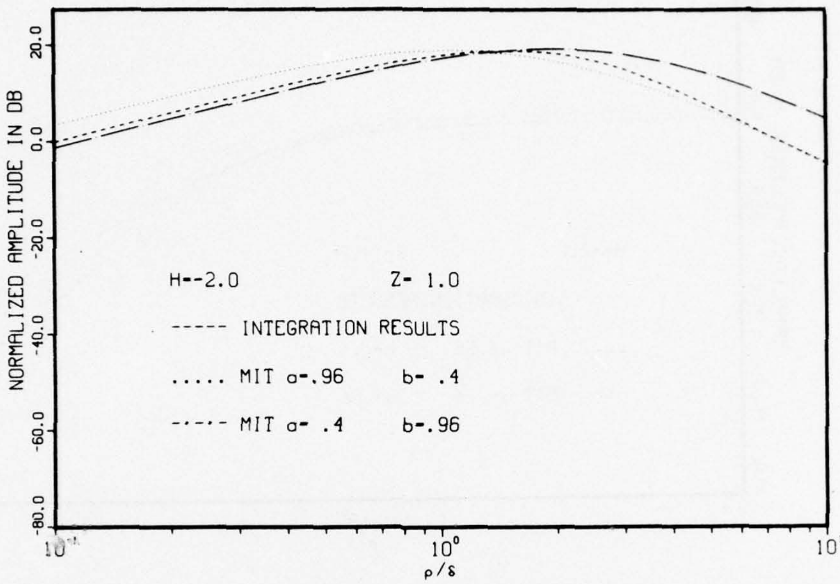

Figure 5. Comparison of Modified Image Theory and Numerical Integration Results for the E_z' Component in Air Produced by a Buried HED (H = -2.0, Z = 1.0)

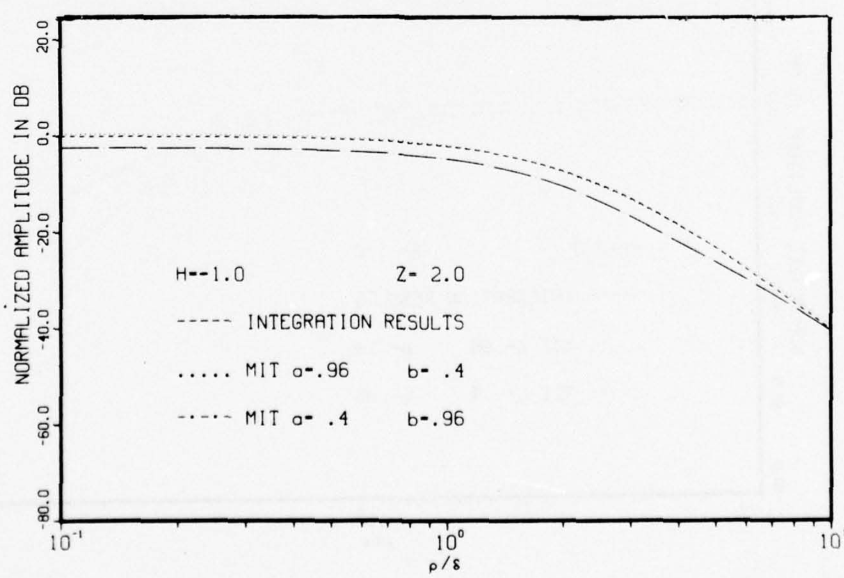

Figure 6. Comparison of Modified Image Theory and Numerical Integration Results for the E_ρ' Component in Air Produced by a Buried HED (H = -1.0, Z = 2.0)

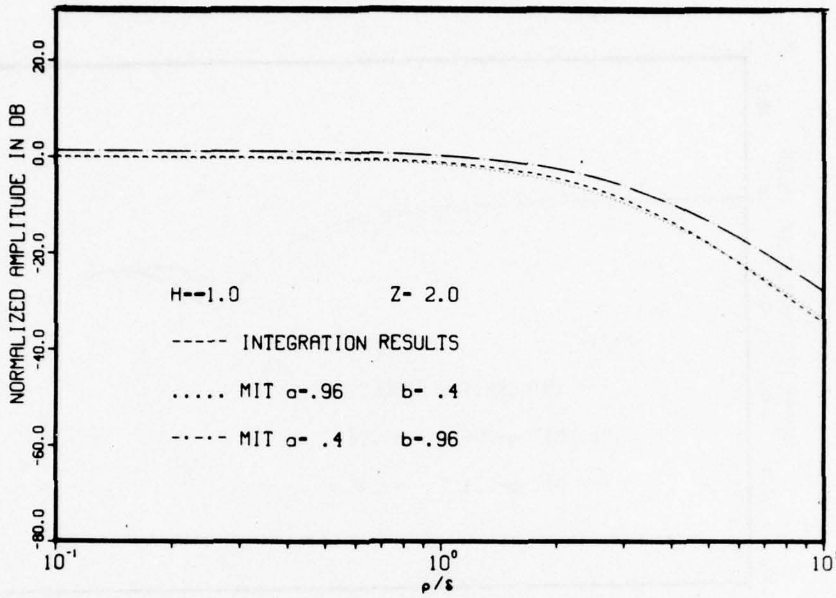

Figure 7. Comparison of Modified Image Theory and Numerical Integration Results for the E_{ϕ}^{a} Component in Air Produced by a Buried HED (H = -1.0, Z = 2.0)

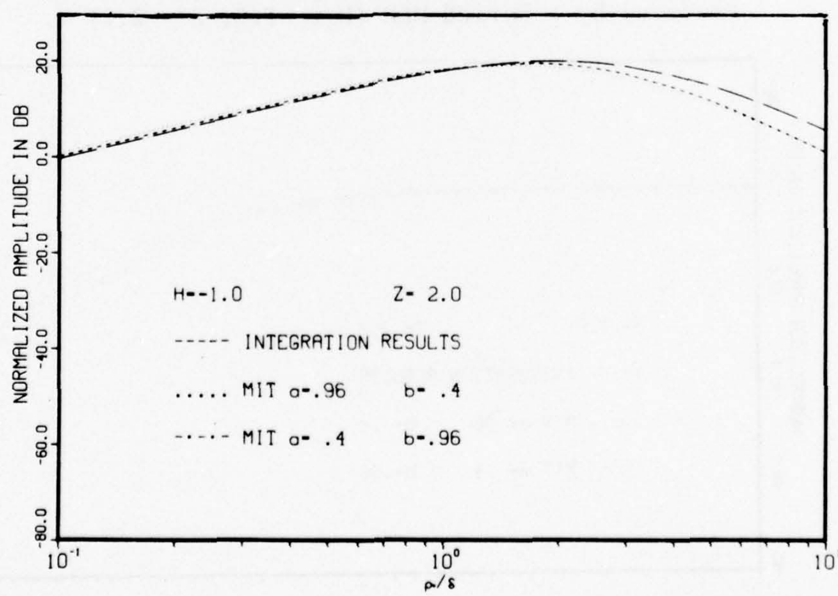

Figure 8. Comparison of Modified Image Theory and Numerical Integration Results for the E_{z}^{a} Component in Air Produced by a Buried HED (H = -1.0, Z = 2.0)

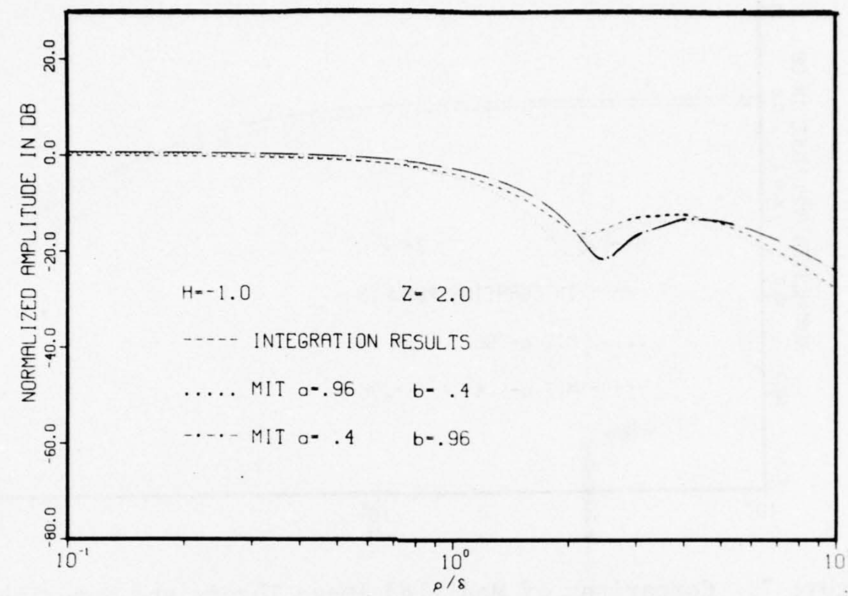

Figure 9. Comparison of Modified Image Theory and Numerical Integration Results for the H_ρ' Component in Air Produced by a Buried HED (H = -1.0, Z = 2.0)

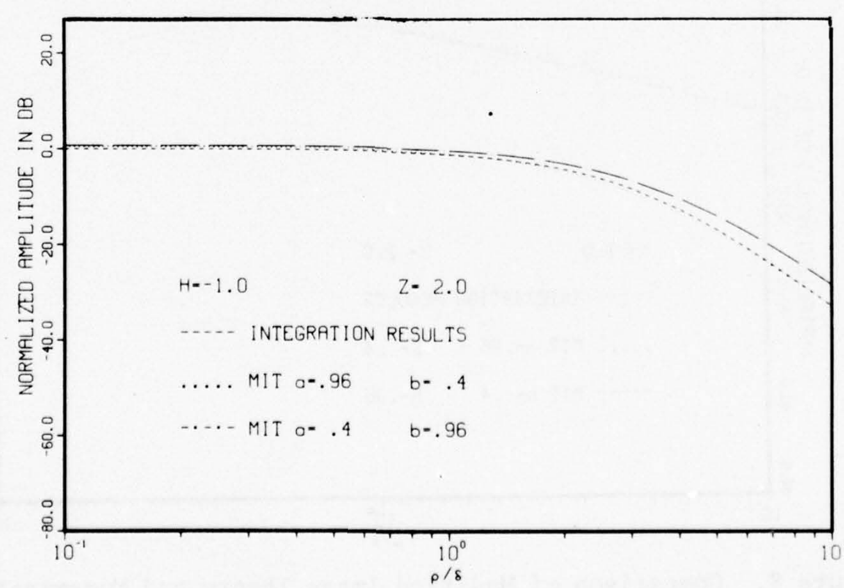

Figure 10. Comparison of Modified Image Theory and Numerical Integration Results for the H_ϕ' Component in Air Produced by a Buried HED (H = -1.0, Z = 2.0)

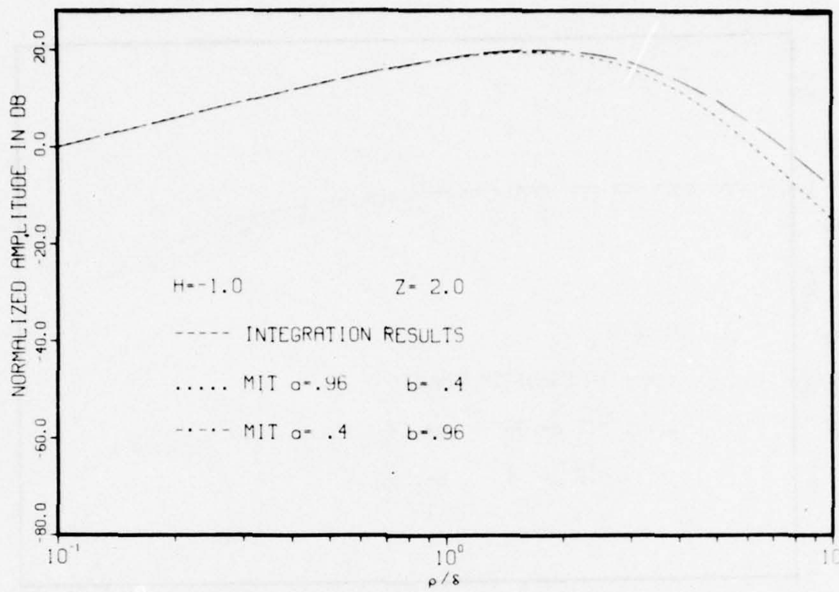

Figure 11. *Comparison of Modified Image Theory and Numerical Integration Results for the* $H_z^{\prime}$ *Component in Air Produced by a Buried HED (H = -1.0, Z = 2.0)*

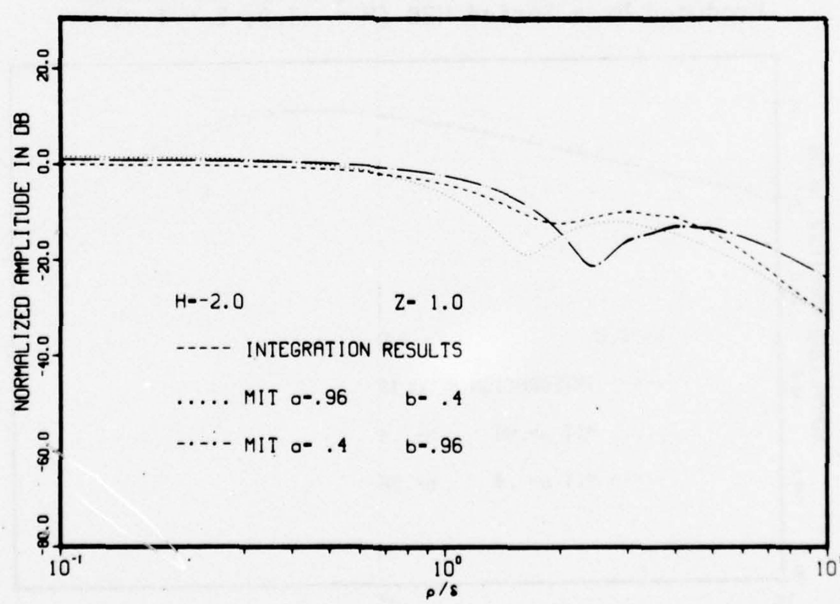

Figure 12. Comparison of Modified Image Theory and Numerical Integration Results for the $H_\rho^{\prime}$ Component in Air Produced by a Buried HED (H = -2.0, Z = 1.0)

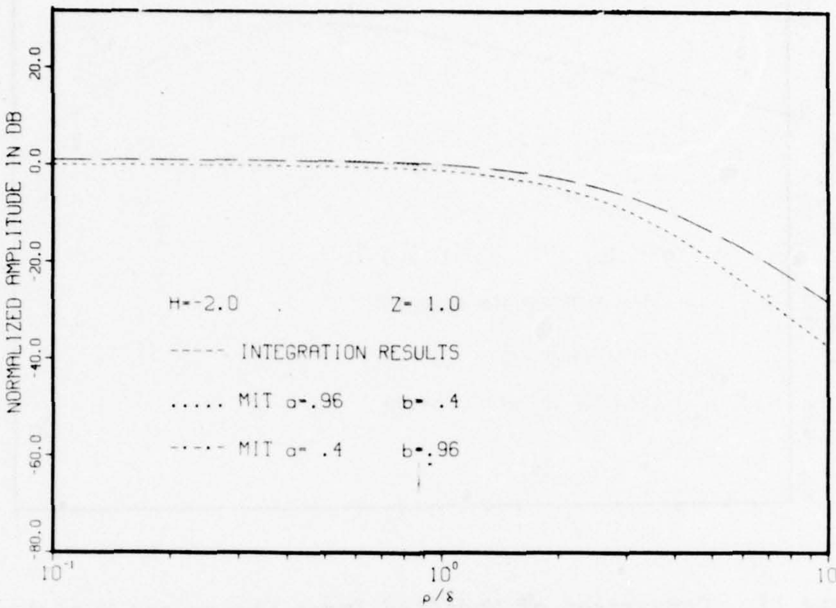

Figure 13. Comparison of Modified Image Theory and Numerical Integration Results for the H_ϕ^s Component in Air Produced by a Buried HED (H = -2.0, Z = 1.0)

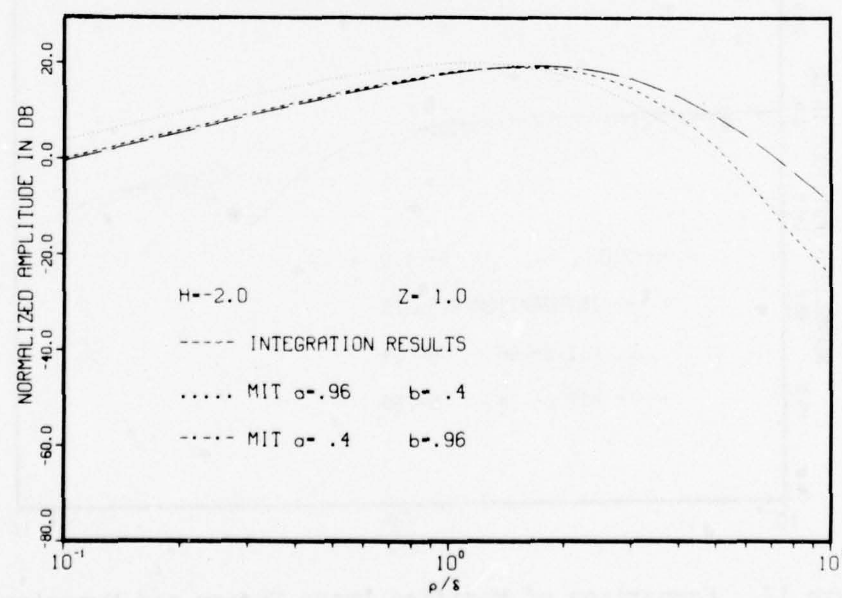

Figure 14. Comparison of Modified Image Theory and Numerical Integration Results for the H_z^s Component in Air Produced by a Buried HED (H = -2.0, Z = 1.0)

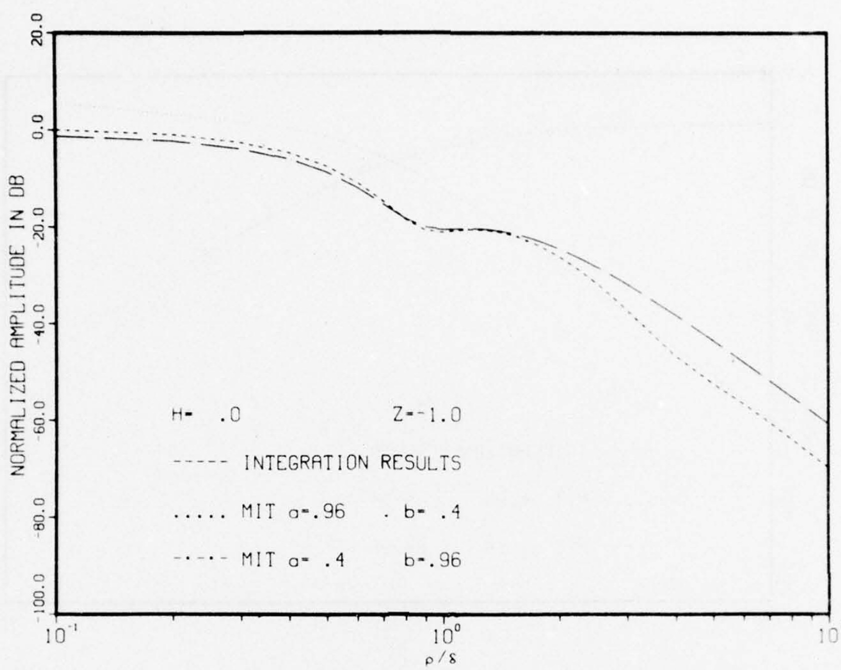

Figure 15. Comparison of Modified Image Theory and Numerical Integration Results for the E'_ρ Component in Earth Produced by a Buried HED ($\hat{H}$ = 0, Z = -1.0)

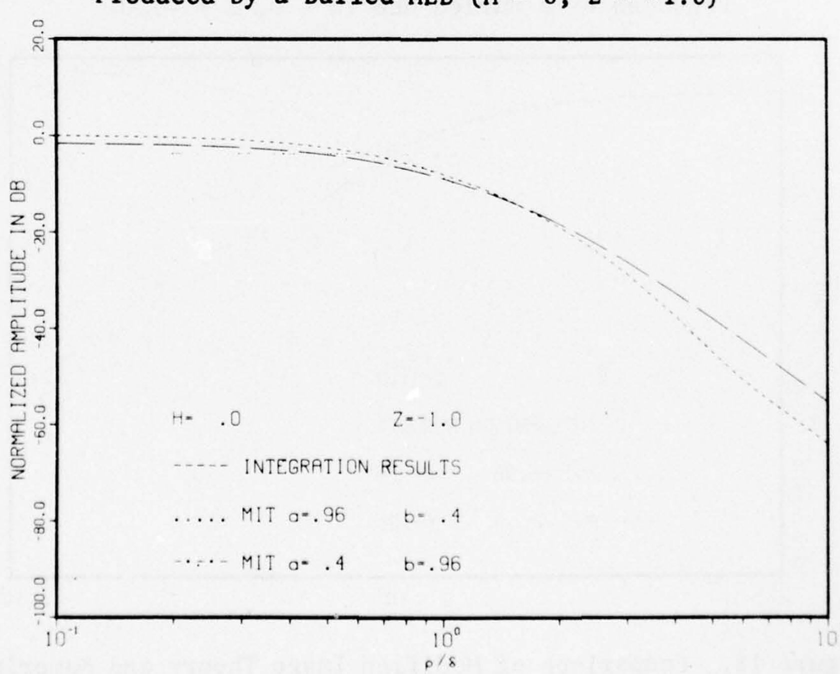

Figure 16. Comparison of Modified Image Theory and Numerical Integration Results for the E'_ϕ Component in Earth Produced by a Buried HED ($\hat{H}$ = 0, Z = -1.0)

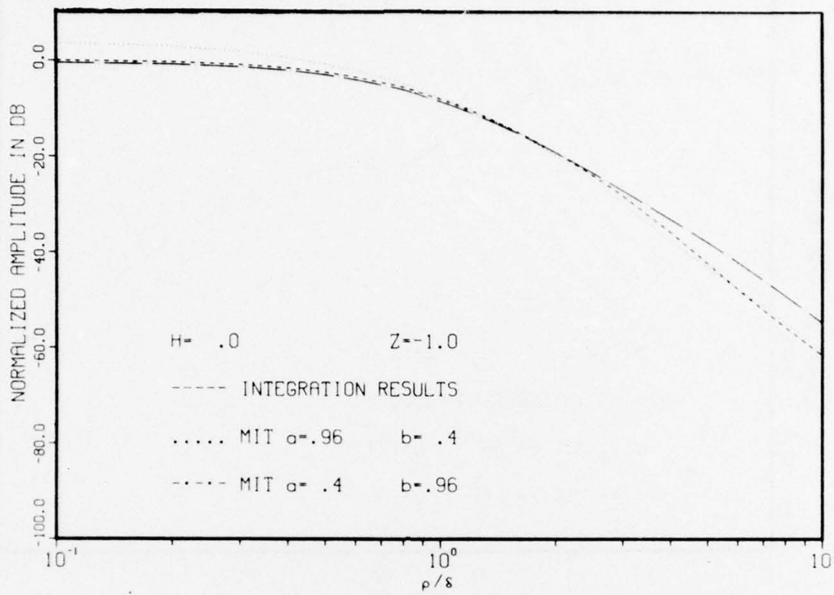

Figure 17. Comparison of Modified Image Theory and Numerical Integration Results for the H'_ρ Component in Earth Produced by a Buried HED (H = 0, Z = -1.0)

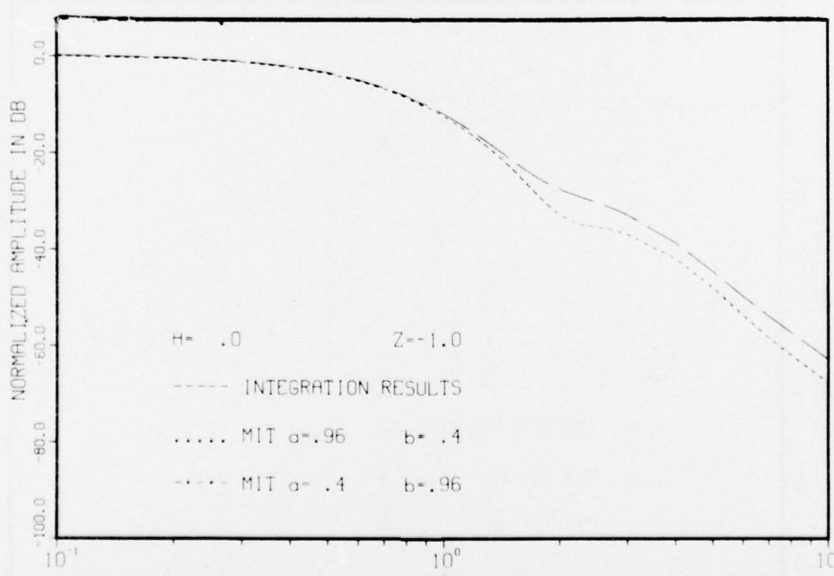

Figure 18. Comparison of Modified Image Theory and Numerical Integration Results for the H'_ϕ Component in Earth Produced by a Buried HED (H = 0, Z = -1.0)

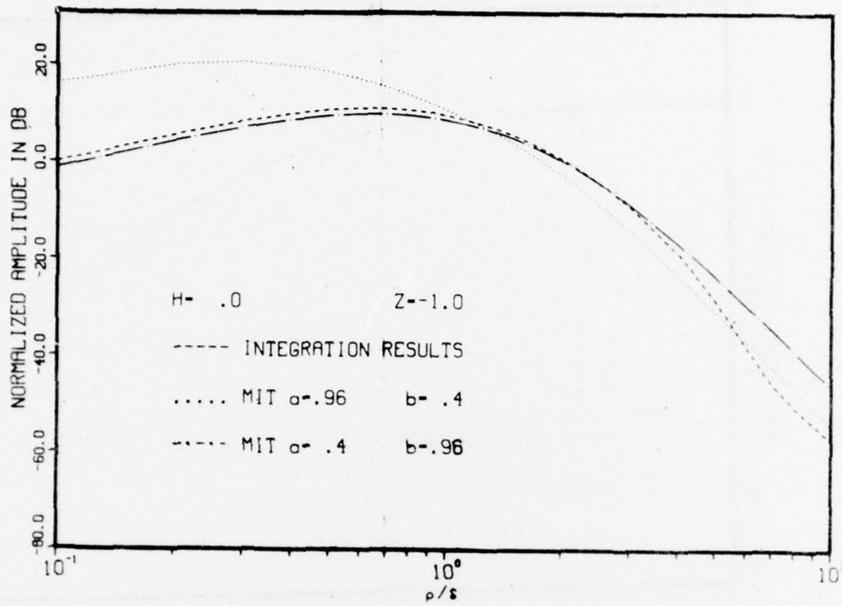

Figure 19. Comparison of Modified Image Theory and Numerical Integration Results for the H_z' Component in Earth Produced by a Buried HED ($H = 0$, $Z = -1.0$)

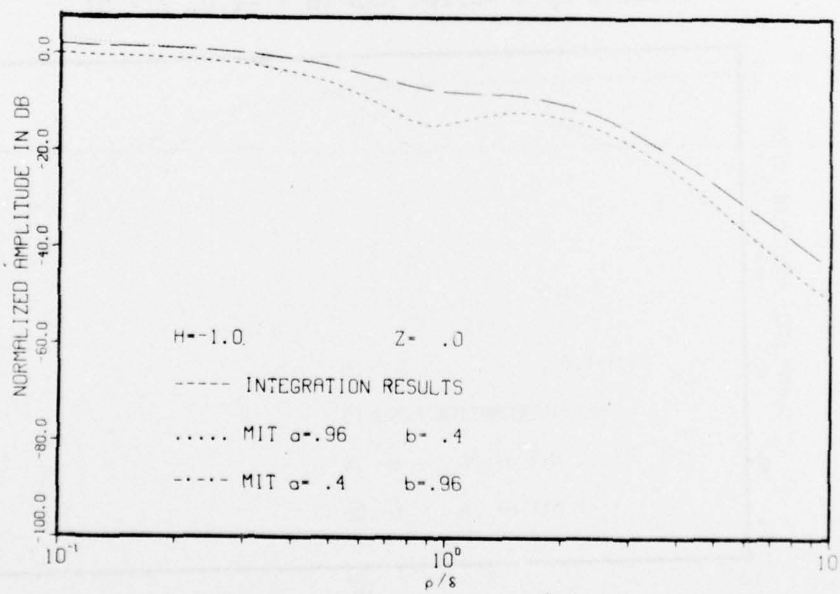

Figure 20. Comparison of Modified Image Theory and Numerical Integration Results for the H_ρ' Component in Earth Produced by a Buried HED ($H = -1.0$, $Z = 0$)

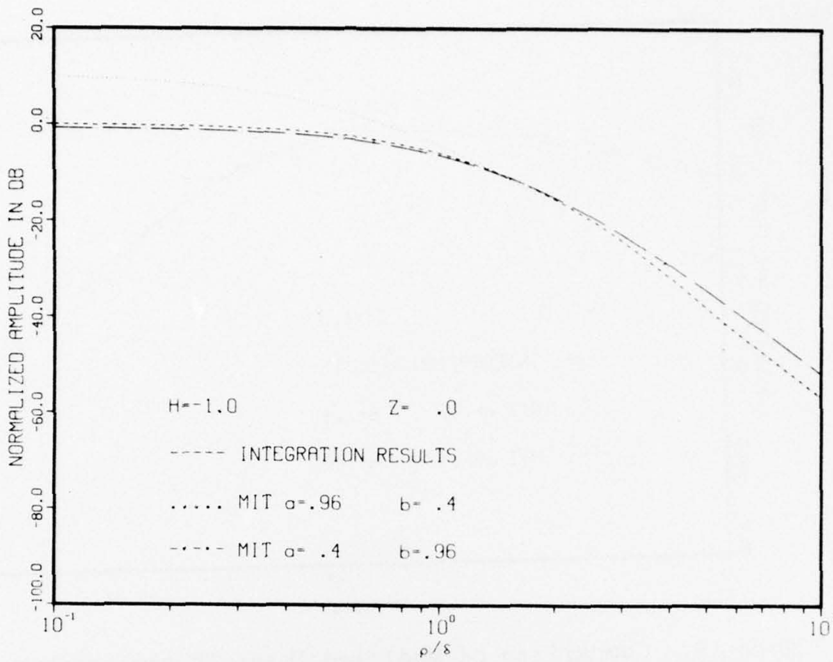

Figure 21. Comparison of Modified Image Theory and Numerical Integration Results for the $H_\phi^{\prime}$ Component in Earth Produced by a Buried HED (H = -1.0, Z = 0)

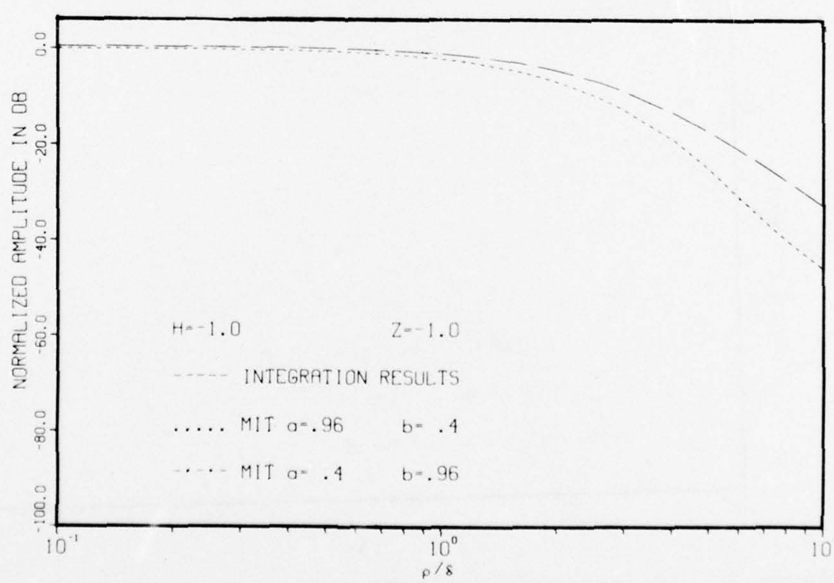

Figure 22. Comparison of Modified Image Theory and Numerical Integration Results for the $H_\rho^{\prime}$ Component in Earth Produced by a Buried HED (H = -1.0, Z = -1.0)

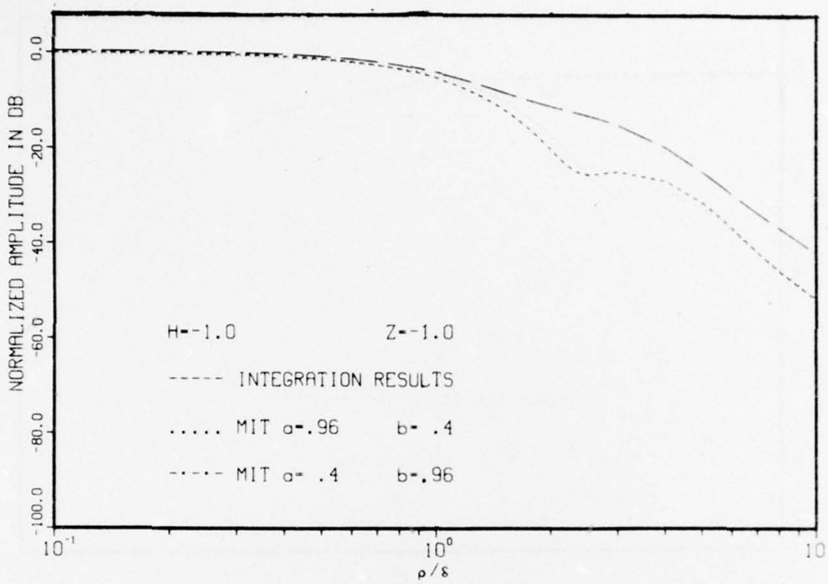

Figure 23. Comparison of Modified Image Theory and Numerical Integration Results for the $H_{\hat{\phi}}$ Component in Earth Produced by a Buried HED (H = -1.0, Z = -1.0)

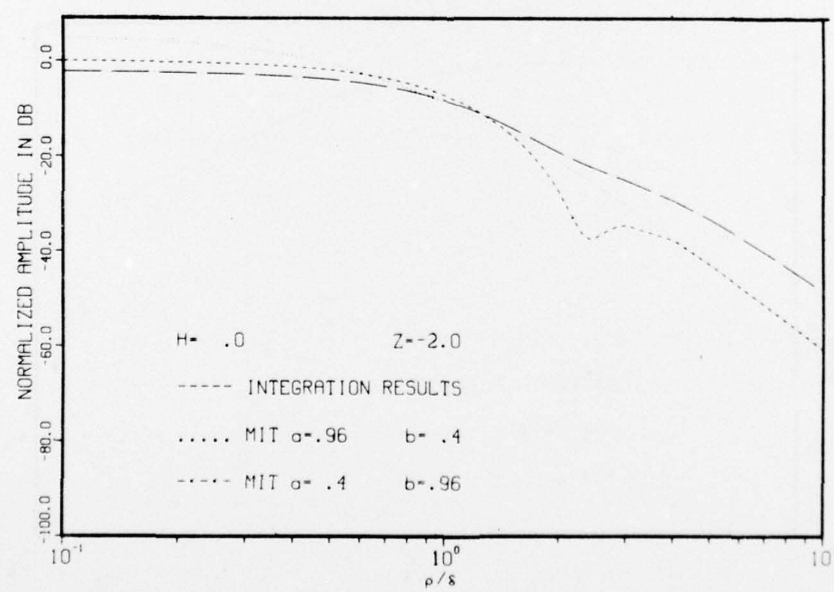

Figure 24. Comparison of Modified Image Theory and Numerical Integration Results for the $E_{\hat{\rho}}$ Component in Earth Produced by a Buried HED (H = 0, Z = -2.0)

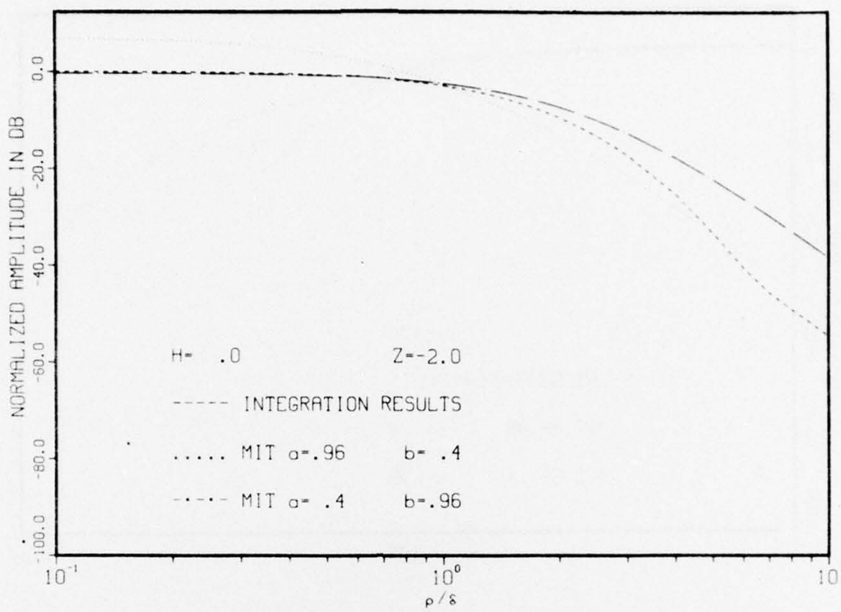

Figure 25. Comparison of Modified Image Theory and Numerical Integration Results for the $E_{\phi}^{\hat{}}$ Component in Earth Produced by a Buried HED (H = 0, Z = -2.0)

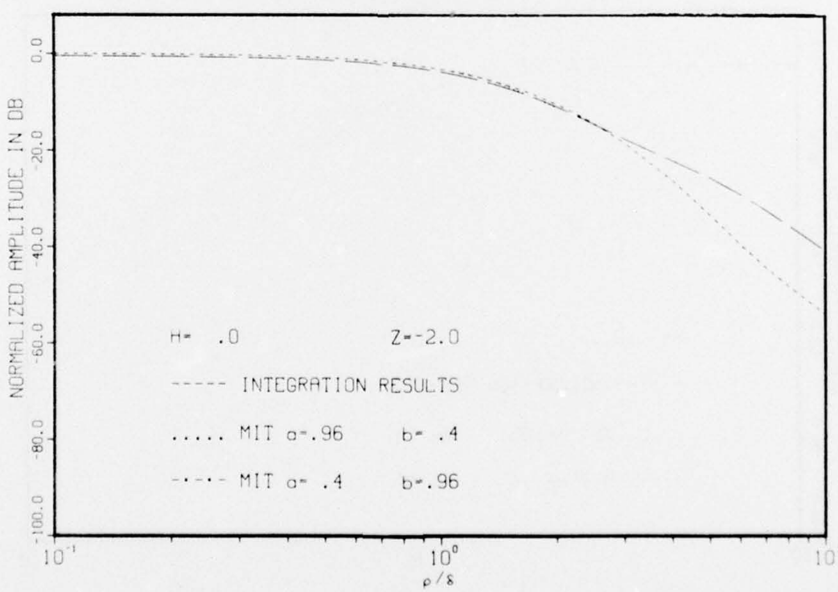

Figure 26. Comparison of Modified Image Theory and Numerical Integration Results for the $H_{\rho}^{\hat{}}$ Component in Earth Produced by a Buried HED (H = 0, Z = -2.0)

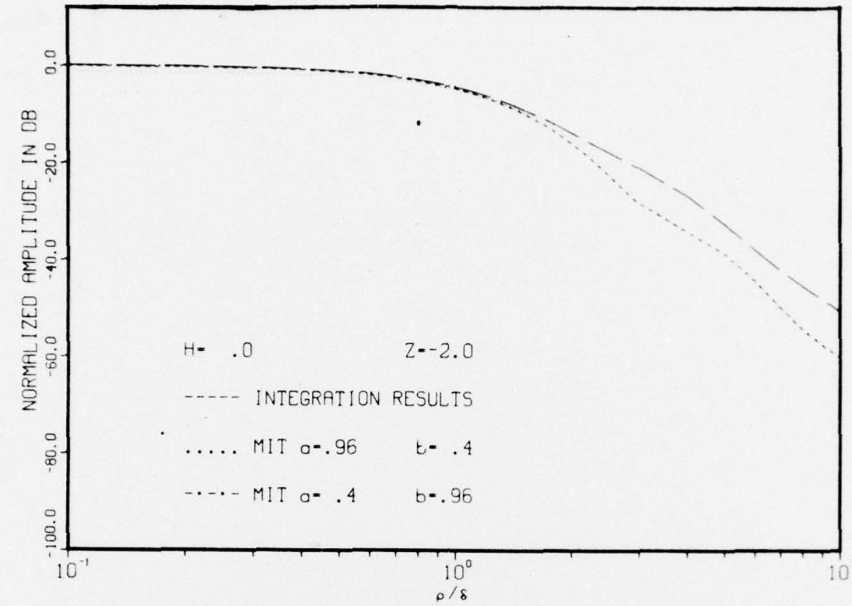

Figure 27. Comparison of Modified Image Theory and Numerical Integration Results for the $H_\phi^{\prime}$ Component in Earth Produced by a Buried HED (H = 0, Z = -2.0)

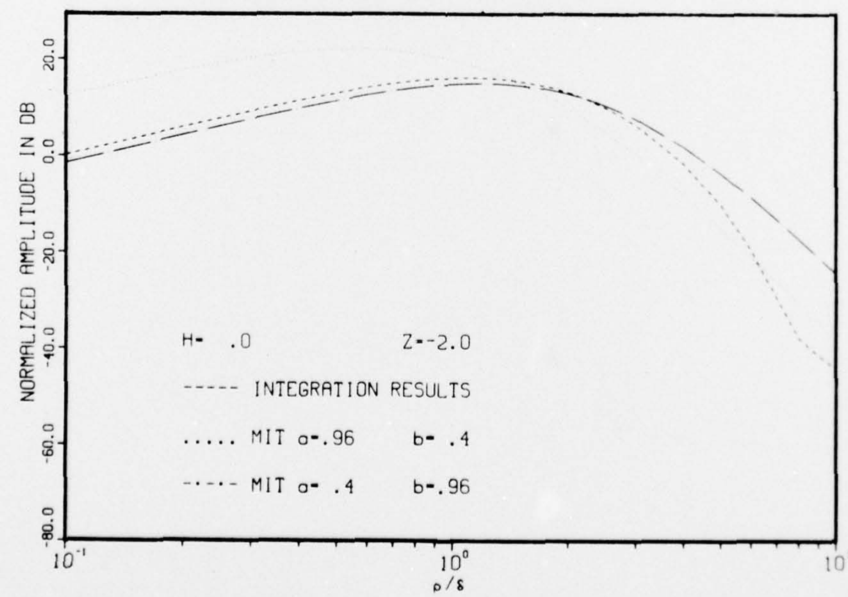

Figure 28. Comparison of Modified Image Theory and Numerical Integration Results for the $H_z^{\prime}$ Component in Earth Produced by a Buried HED (H = 0, Z = -2.0)

REFERENCES

1. J. R. Wait, "The Electromagnetic Fields of a Horizontal Dipole in the Presence of a Conducting Half-Space," Canadian Journal of Physics, vol. 39, 1961, pp. 1017-1028.

2. J. R. Wait and L. L. Campbell, "The Fields of an Electric Dipole in a Semi-Infinite Conducting Medium," Journal of Geophysical Research, vol. 58, 1953, pp. 21-28.

3. J. R. Wait and L. L. Campbell, "The Fields of an Oscillating Magnetic Dipole Immersed in a Semi-Infinite Conducting Medium," Journal of Geophysical Research, vol. 58, no. 2, 1953, pp. 167-178.

4. A. H. Sinha and P. K. Bhattacharya, "Vertical Magnetic Dipole Buried Inside a Homogeneous Earth," Radio Science, vol. 1, no. 3, 1966, pp. 379-395.

5. P. R. Bannister and W. C. Hart, Quasi-Static Fields of Dipole Antennas Below the Earth's Surface, NUSL Technical Report 870, 11 April 1968.

6. E. M. Atzinger, A. F. Pensa, and M. T. Pigott, "On the Application of a Calculation by Wait and Campbell: The Fields of an Oscillating Magnetic Dipole Immersed in a Semi-Infinite Conducting Medium," Journal of Geophysical Research, vol. 71, no. 23, 1966, pp. 5765-5769.

7. A. C. Fraser-Smith and D. M. Bubenik, "ULF/ELF Magnetic Fields Generated at the Sea Surface by Submerged Magnetic Dipoles," Radio Science, vol. 11, no. 11, 1976, pp. 901-913.

8. A. C. Fraser-Smith, D. M. Bubenik, and O. G. Villard, Jr., Air/Undersea Communications at Ultra-Low Frequencies Using Airborne Loop Antennas, Radioscience Laboratory, Stanford Electronics Laboratories Technical Report No. 4207-6, June 1977.

9. P. R. Bannister and R. L. Dube, Modified Image Theory Quasi-Static Range Subsurface-to-Subsurface and Subsurface-to-Air Propagation Equations, NUSC Technical Report 5647, 12 October 1977.

10. P. R. Bannister, The Image Theory Quasi-Static Fields of Antennas Above the Earth's Surface, NUSL Technical Report 1061, 29 December 1969.

REFERENCES (Cont'd)

11. D. J. Thomson and J. T. Weaver, "The Complex Image Approximation for Induction in a Multilayered Earth," Journal of Geophysical Research, vol. 80, 1975, pp. 123-129.

12. M. B. Kraichman, Handbook of Electromagnetic Propagation in Conducting Media, U. S. Government Printing Office, Washington, DC, 1970 (second edition, 1976).

INITIAL DISTRIBUTION LIST

Addressee	No. of Copies
ONR, Code 427, 483, 412-8, 480, 410, Earth Sciences Division (T. Quinn))	6
ONR Branch Office, Chicago (F. L. Dowling)	1
NRL, (J. Davis, W. Meyers, R. Dinger, F. Kelly), Code 6451 (D. Forester), 6454 (J. Clement, E. Compy, P. Lubitz, J. Schelleng)	9
NAVELECSYSCOMHQ, Code 03, PME-117, -117-21, -117-213, -117-213A, -117-215	6
NELC, (R. Moler, H. Hughes, R. Pappert, Code 3300)	4
NAVMAT, Code PM2-00 (RADM J. Metzel, Jr.), PM2-001 (J. Crone)	2
NAVSEASYSCOMHQ, Code SEA-03424 (W. Welsh), -0227 (J. Fox), -03C, -034, -06H, -660C, -660D, PMS-396	8
DTNSRDC/A, Code 2782 (W. Andahazy, L. Dadin, D. Everstine, B. Hood, D. Nixon, D. Peoples, T. Shaw, F. Walker), 2732 (F. Baker, D. Fairhead), 2813 (E. Bieberich), 278 (H. Boroson), 2733 (P. Field, D. Rockwell), 0700 (R. Robinson)	15
DTNSRDC/C, Code 1548 (R. Knutson), 1102.2 (J. Stinson)	2
NAVSURFWPNCEN, Code WE-04 (W. Stoll, D. Norton), -12 (K. Bishop, M. Lackey, Jr., W. Menzel, J. Miller, E. Peizer, R. Stabnow, G. Stimak, J. Whelan), WR-43 (R. Brown, J. Cunningham, Jr., M. Kraichman, G. Usher)	14
NAVCOASTSYSLAB, Code 721 (C. Stewart), 773 (K. Allen), 792 (M. Wynn, W. Wynn)	4
NAVSEC, Code 6157 B (C. Butler, G. Kahler, D. Muegge)	3
NAVFACENGSYSCOM, Code FPO-1C (W. Sherwood), -1C7 (R. McIntyre, A. Sutherland)	3
NAVAIR, Code AIR-0632 B (L. Goertzen)	1
NAVAIRDEVCEN, Code 2022 (J. Duke, R. Gasser, E. Greeley, A. Ochadlick, L. Ott, W. Payton, W. Schmidt)	7
NAVSHIPYD PTSMH, Code 280 (B. Murdock)	1
AFWTF, Code 01A (CDR W. Danner), 32 (LT R. Elston), 412 (P. Burton, R. Kirkpatrick)	4
NISC, Code 20 (G. Batts), 43 (J. Erdmann), OW17 (M. Koontz)	3
NOSC, Code 407 (C. Ramstedt)	1
NAVPGSCOL, Code 06 (R. Fossum)	1
U. S. Naval Academy, Anna. (C. Schneider)	1
CNO, Code OP-02, 03EG, -090, -23, -902, 941, -942U, 201, -953, -954, -96	11
CNM, Code MAT-00, -03L, -0302, -034, -03T (CAPT Walker), ASW-23	6
SUBASE LANT	1

INITIAL DISTRIBUTION LIST (Cont'd)

Addressee	No. of Copies
NAVSUBSUPFACNLON	1
NAVWPNSCEN	1
NAVSUBTRACENPAC	1
CIVENGRLAB	1
NAVSUBSCOL	1
NAVWARCOL	1
DDC, Alexandria	12
Engineering Societies Library United Engineering Center 345 East 47th St. New York, NY 10017	1
GTE Sylvania (G. Pucillo, D. Esten, R. Warshamer, D. Boots, R. Row) Needham, MA 02194	5
Lockheed (J. Reagan, W. Imhof, T. Larsen) Palo Alto, CA 94302	3
Lawrence Livermore Labs (J. Lytle, E. Miller) Livermore, CA 94550	2
Ratheon Co. (J. de Bettencourt) Norwood, MA 02062	1
Univ. of Nebraska Dept. of EE (E. Bahar) Lincoln, NB 68508	1
NOAA (D. Barrick, R. Fitzgerrell, D. Grubb, J. Wait (ERL)) U.S. Dept. of Commerce Boulder, CO 80302	4
Newmont Exploration Ltd. (A. Brant) Danbury, CT 06810	1

INITIAL DISTRIBUTION LIST (Cont'd)

Addressee	No. of Copies
IITRI (J. Bridges) Chicago, IL 60068	1
Stanford Univ. Dept. of EE (F. Crawford) Stanford, CA 94305	1
Stanford Univ. P.O. Box 7457 (J. Wikswo) Menlo Park, CA 94025	1
Univ. of Colorado Dept. of EE (D. Chang) Boulder, CO 80302	1
SRI (L. Dolphin, Jr., A. Fraser-Smith, J. Chown, R. Honey, M. Morgan) Menlo Park, CA 94025	5
Air Force Cambridge Research Lab (R. Fante) Bedford, MA 01730	1
USGS - Federal Centre Regional Geophysics Branch (F. Frischknecht) Denver, CO 80225	1
Colorado School of Mines Geophysics Dept. (R. Geyer, G. Keller) Golden, CO 80401	2
Univ. of Arizona Dept. of Mining & Geological Engineering (D. Hastings) Tuscon, AZ 85721	1
Univ. of Michigan Radiation Lab (R. Hiatt) Ann Arbor, MI 48105	1

INITIAL DISTRIBUTION LIST (Cont'd)

Addressee	No. of Copies
U. S. Army Cold Regions Research & Eng. Lab (P. Hoekstra) Hanover, NH 03755	1
Univ. of Washington Dept. of EE (A. Ishimaru) Seattle, WA 98105	1
Univ. of Wisconsin Dept. of EE (R. King) Madison, WI 53706	1
Univ. of Wyoming Dept. of EE (J. Lindsay, Jr.) Laramie, WY 82070	1
Univ. of Arizona College of Earth Sciences (L. Lepley) Tucson, AZ 85719	1
Univ. of Illinois Dept. of EE (R. Mittra) Urbana, IL 61801	1
Univ. of Kansas (R. Moore) Lawrence, KS 66044	1
Washington State Univ. Dept. of EE (R. Olsen) Pullman, WA 99163	1
Institute for Telecommunication Services U.S. Dept. of Commerce (R. Ott) Boulder, CO 80302	1
North Carolina State Univ. Dept. of EE (R. Rhodes) Raleigh, NC 27607	1

INITIAL DISTRIBUTION LIST (Cont'd)

Addressee	No. of Copies
Ohio State Univ. Dept. of EE (J. Richmond) Columbus, OH 43212	1
MIT Lincoln Laboratory (J. Ruze, D. White, J. Evans, A. Griffiths, L. Ricardi) Lexington, MA 02137	5
Univ. of Utah Dept. of Geological & Geophysical Sciences (S. Ward) Salt Lake City, UT 84112	1
Purdue Univ. School of EE (W. Weeks) Lafayette, IN 47907	1
Nat'l Oceanographic & Atmospheric Admin. Wave Propagation Lab (G. Little) Boulder, CO 80302	1
Univ. of Pennsylvania Moore School of EE D2 (R. Showers) Philadelphia, PA 19174	1
Dynatrend Incorporated (F. Ostherr, L. Parente) Burlington, MA 01803	2
Dynatrend Incorporated/DC (E. Mansfield) Arlington, VA 22209	1
Cadcom Incorporated (D. Brake, W. Hicks, F. Klappenberger, N. Nicholas) Annapolis, MD 21401	4
Electric Boat Division (R. Clark, L. Conklin, H. Hemond, G. McCue, D. Odryna) Groton, CT 06340	5

INITIAL DISTRIBUTION LIST (Cont'd)

Addressee	No. of Copies
Science Application Incorporated (J. Czika) McLean, VA 22101	1
JHU/APL (W. Chambers, P. Gueschel, L. Hart, H. Ko) Silver Spring, MD 20910	4
SACLANT ASW Research Centre	1